Weierstraß-Institut
für Angewandte Analysis und Stochastik

Leibniz-Institut im Forschungsverbund Berlin e. V.

Preprint ISSN 2198-5855

Comparison of monomorphic and polymorphic approaches for uncertainty quantification with experimental investigations

Martin Drieschner[1], Martin Eigel[2], Robert Gruhlke[2],

Dietmar Hömberg[2], Yuri Petryna[1]

submitted: March 1, 2019

[1] Technische Universität Berlin
Department of Civil Engineering
Gustav-Meyer-Allee 25
13355 Berlin
Germany
E-Mail: martin.drieschner@tu-berlin.de
yuriy.petryna@tu-berlin.de

[2] Weierstrass Institute
Mohrenstr. 39
10117 Berlin
Germany
E-Mail: martin.eigel@wias-berlin.de
robert.gruhlke@wias-berlin.de
dietmar.hoemberg@wias-berlin.de

No. 2579
Berlin 2019

2010 *Mathematics Subject Classification.* 35R13, 35R60, 60H35, 65C20, 65N12, 65N22, 65J10, 74B05.

Key words and phrases. Structural failure, experimental and numerical investigations, monomorphic uncertainty modeling, polymorphic uncertainty modeling, artificial neural networks, fuzzy, uncertainty quantification, elasticity.

The authors gladly acknowledge the funding of Martin Drieschner and Robert Gruhlke in the DFG SPP 1886 “Polymorphic uncertainty modelling for the numerical design of structures”.

Edited by
Weierstraß-Institut für Angewandte Analysis und Stochastik (WIAS)
Leibniz-Institut im Forschungsverbund Berlin e. V.
Mohrenstraße 39
10117 Berlin
Germany

Fax: +49 30 20372-303
E-Mail: preprint@wias-berlin.de
World Wide Web: http://www.wias-berlin.de/

Comparison of monomorphic and polymorphic approaches for uncertainty quantification with experimental investigations

Martin Drieschner, Martin Eigel, Robert Gruhlke,
Dietmar Hömberg, Yuri Petryna

Abstract

Unavoidable uncertainties due to natural variability, inaccuracies, imperfections or lack of knowledge are always present in real world problems. To take them into account within a numerical simulation, the probability, possibility or fuzzy set theory as well as a combination of these are potentially usable for the description and quantification of uncertainties. In this work, different monomorphic and polymorphic uncertainty models are applied on linear elastic structures with non-periodic perforations in order to analyze the individual usefulness and expressiveness. The first principal stress is used as an indicator for structural failure which is evaluated and classified. In addition to classical sampling methods, a surrogate model based on artificial neural networks is presented. With regard to accuracy, efficiency and resulting numerical predictions, all methods are compared and assessed with respect to the added value. Real experiments of perforated plates under uniaxial tension are validated with the help of the different uncertainty models.

1 Introduction

This study has been performed within the research project MuScaBlaDes – „Multi-scale failure analysis with polymorphic uncertainties for optimal design of rotor blades“ – which is part of the DFG Priority Programme (SPP 1886) „Polymorphic uncertainty modelling for the numerical design of structures“.

Air void inclusions are unavoidable in many different materials resulting from manufacturing processes or environmental conditions which lead to stress concentrations around them [9], see [18] for an extensive overview with a broad spectrum of investigations. They can influence significantly the structural integrity and in the worst case lead to structural failure.

For numerical investigations on the stress concentration and resulting structural failure, a 2D linear elastostatic boundary value problem for a perforated structure is defined in Section 2. The first principal stress is used as an indicator for structural failure which is evaluated and classified.

Two different perforated Plexiglas® plates with previously determined material properties were loaded experimentally by uniaxial tension, see Section 3.

The discrepancy between experimental results and deterministic numerical predictions leads to a problem description under uncertainties. Monomorphic models including probabilistic [12, 21] (stochastic) and possibilistic [8, 19] (in terms of fuzzy arithmetic) techniques as well as a polymorphic model [7, 14, 20] in the sense of a hybrid fuzzy-stochastic framework are presented in Section 4. Furthermore, a surrogate model based on artificial neural networks [6] is defined to overcome the computational costly uncertainty propagations.

The application of the different monomorphic and polymorphic uncertainty models is given in Section 5. The individual usefulness and expressiveness are analyzed and the methods are compared

DOI 10.20347/WIAS.PREPRINT.2579 Berlin 2019

with regard to accuracy, efficiency and resulting numerical prediction.

Finally, conclusions and an outlook on the ongoing work are given in Section 6.

2 Deterministic elastic model for perforated bodies

Consider a (deterministic) linear elastostatic equation on a perforated reference body denoted by $D_{\mathcal{P}} \subset D \subset \mathbb{R}^d$, $d = 2$, an unperforated LIPSCHITZ domain D. In addition, a finite number of sets $\mathcal{E}_i \subset \mathbb{R}^d$, $i \in I := \{1, \dots, N_I\}$ and $\mathcal{L}_j \subset \mathbb{R}^d$, $j \in J := \{1, \dots, N_J\}$ is defined for $N_I, N_J \in \mathbb{N}$ representing elliptical and slotted holes as specified in Table 1 and as displayed in Figure 1. Denote by $\mathcal{P}$ a set of perforations given as possible union of elliptical and slotted holes defined for $N_{\mathcal{P}} \leq N_I + N_J$ by

$$\mathcal{P} := \{P_k \,|\, k = 1, \dots, N_{\mathcal{P}}\}, \quad P_k = \bigcup_{i \in I_k \subset I} \mathcal{E}_i \cup \bigcup_{j \in J_k \subset J} \mathcal{L}_j, \tag{1}$$

for disjoint index sets $\{I_k\}$ and $\{J_k\}$. s.t. $\dot{\bigcup}_{k=1}^{N_{\mathcal{P}}} I_k = I$ and $\dot{\bigcup}_{k=1}^{N_{\mathcal{P}}} J_k = J$. The perforated domain is defined as

$$D_{\mathcal{P}} := D \setminus \overline{\cup_{P \in \mathcal{P}} P}. \tag{2}$$

When $\boldsymbol{a} = (a_1, a_2) = (w/2, w/2)$ and $\ell = w$ the elliptical or slotted hole becomes a circular perforation labeled as $\mathcal{B}$ with simplified parameterization via midpoint $\boldsymbol{M}$ and diameter d defining $\boldsymbol{a} = (d/2, d/2)$.

Table 1: Considered perforations for $d = 2$ specified by their parameters.

perforation	elliptical hole $\mathcal{E}$	slotted hole $\mathcal{L}$
parameters	midpoint, stretch, rotation	midpoint, length, width, rotation
max. range	$(\boldsymbol{M}, \mathbf{a}, \theta) \in D \times \mathbb{R}^d_+ \times [0, 2\pi)$	$(\boldsymbol{M}, \ell, w, \theta) \in D \times \mathbb{R}_+ \times \mathbb{R}_+ \times [0, 2\pi)$

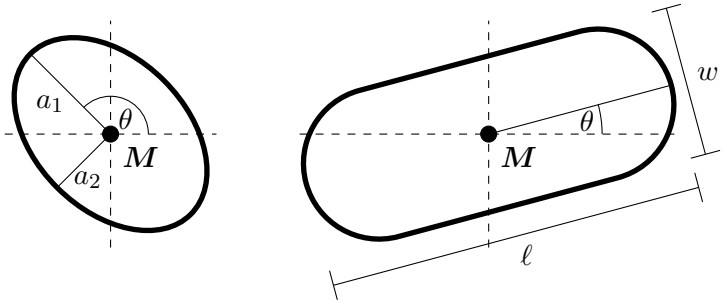

Figure 1: Illustration of involved perforations and its related parameters with $\boldsymbol{a} = (a_1, a_2)$.

The maximum ranges of the parameters are constrained due to the following assumptions on $\mathcal{P}$:

$(\mathbf{A1})$ Each perforation $\mathcal{P}_k \in \mathcal{P}$ has an intersection with D of positive measure, $|\mathcal{P}_k \cap D| > 0$.

$(\mathbf{A2})$ All perforations in $\mathcal{P}$ are either piecewise disjoint with an uniform prescribed EUCLIDIAN distance of at least $\delta > 0$ or they overlap such that $D_{\mathcal{P}}$ remains LIPSCHITZian.

$(\mathbf{A3})$ All perforations in $\mathcal{P}$ are bounded away from ∂D with distance at least $\delta > 0$.

Then the linear elasticity boundary value problem of interest in strong form in $D_{\mathcal{P}}$ reads

$$\left\{\begin{array}{rcll} \boldsymbol{f} &=& -\operatorname{div}\boldsymbol{\sigma} & \text{equilibrium equation} \\ \boldsymbol{\epsilon} &=& \left[\nabla\boldsymbol{u} + \nabla^T\boldsymbol{u}\right]/2 & \text{strain-displacement equation} \\ \boldsymbol{\sigma} &=& \boldsymbol{C} : \boldsymbol{\epsilon} & \text{constitutive equation} \\ \boldsymbol{u} &=& \mathbf{0} & \text{Dirichlet boundary conditions} \\ \boldsymbol{\sigma}\cdot\boldsymbol{n} &=& \boldsymbol{h} & \text{Neumann boundary conditions} \\ \boldsymbol{\sigma}\cdot\boldsymbol{n} &=& \mathbf{0} & \text{Neumann boundary conditions} \end{array}\right. \begin{array}{l} \left.\begin{array}{l} \\ \\ \\ \end{array}\right\} \text{ in } D_{\mathcal{P}}, \\ \text{on } \Gamma_{\mathbf{0}} \subset \partial D, \\ \text{on } \Gamma_{\boldsymbol{\sigma}} := \partial D \setminus \Gamma_{\mathbf{0}}, \\ \text{on } \Gamma_{\boldsymbol{\sigma},\mathbf{0}} := \partial\overline{\cup_{P\in\mathcal{P}} P}. \end{array} \tag{3}$$

Let $|\Gamma_{\mathbf{0}}| > 0$ and assumption $(\mathbf{A1}) - (\mathbf{A3})$ hold true. Furthermore, let the data $\boldsymbol{C}, \boldsymbol{f}$ and $\boldsymbol{h}$ be regular enough such that the LAX-MILGRAM theorem applies to ensure existence and uniqueness of a (weak) solution $\boldsymbol{u} \in V := H^1_{\Gamma_{\mathbf{0}}}(D_{\mathcal{P}})^d$ solving the variational formulation

$$\int_D \boldsymbol{\sigma}(\boldsymbol{u}) : \nabla\boldsymbol{v}\,\mathrm{d}\boldsymbol{x} = \int_D \boldsymbol{f}\cdot\boldsymbol{v}\,\mathrm{d}\boldsymbol{x} + \int_{\Gamma_\sigma} \boldsymbol{h}\cdot\boldsymbol{v}\mathrm{dS}, \quad \text{for all } \boldsymbol{v} \in V. \tag{4}$$

Consider the case of an isolated perforation $P \in \mathcal{P}$ and assume that $\boldsymbol{C}$ is constant and $\boldsymbol{f}$ smooth in a neighbourhood of P. Then, due to the smoothness of ∂P in that neighbourhood, C^1 regularity holds for $\boldsymbol{u}$ [4] and consequently pointwise $\boldsymbol{\sigma}(\boldsymbol{u})[\boldsymbol{x}]$ is well-defined in that neighbourhood. For a qualitative and quantitative comparison with experimentally determined failure mechanisms and ultimate loads the computation of the maximum first principal stress and of its location is of interest:

$$\sigma_{1,\max} = \operatorname*{ess\,sup}_{\boldsymbol{x}\in D_{\mathcal{P}}} \lambda_{\max}(\boldsymbol{\sigma}(\boldsymbol{u})[\boldsymbol{x}]), \tag{5}$$

$$\boldsymbol{x}_{\max} = \operatorname*{arg\,max}_{\boldsymbol{x}\in D_{\mathcal{P}}} \sigma_{1,\max}. \tag{6}$$

Here $\lambda_{\max}(A)$ denotes the largest eigenvalue of a matrix A. The *structural failure* is reached if $\sigma_{1,\max}$ in the structure exceeds the tensile strength f_{t}. This criterion leads to the assumption that the first crack location is equivalent to $\boldsymbol{x}_{\max}$.

For the application in mind the 2D model is derived from a 3D model of a thin Plexiglas® cuboid ($L \times W \times T$) with $T \ll L, W$ s.t. $D = [0, L] \times [0, W]$ is modeled rectangular with $\Gamma_{\mathbf{0}} = \{0\} \times [0, W]$, see Figure 2. Based on the calculated stress concentration, the given tensile strength and the geometrical dimensions the ultimate load $F_{\max}$ is calculated by

$$F_{\max} = \frac{\sigma_{\mathrm{N}}}{\sigma_{1,\max}} f_{\mathrm{t}} WT \in [0; f_{\mathrm{t}} WT] \tag{7}$$

with uniaxial loading $\sigma_{\mathrm{N}} = \|\boldsymbol{h}(\boldsymbol{x}_{\max})\|_2$. Furthermore $\boldsymbol{f}$ is modeled as $\boldsymbol{f} \equiv 0$ and $\boldsymbol{h}$ as piecewise constant s.t.

$$\boldsymbol{h} = \left\{\begin{array}{ll} Q[\alpha_{\mathrm{F}}]\boldsymbol{e}_1, & \text{on } \Gamma^r_{\boldsymbol{\sigma}} := \{L\} \times [0, W] \subset \Gamma_{\boldsymbol{\sigma}}, \\ \mathbf{0}, & \text{on } \Gamma_{\boldsymbol{\sigma}} \setminus \Gamma^r_{\boldsymbol{\sigma}}, \end{array}\right. \tag{8}$$

with a rotation matrix $Q[\alpha_{\mathrm{F}}]$ with deterministic load angle $\alpha_{\mathrm{F}} = 0$ and $\boldsymbol{e}_1 = (1, 0)^T$. The material response is encoded in a constant stiffness tensor $\boldsymbol{C} = \lambda \boldsymbol{I}_2 \otimes \boldsymbol{I}_2 + 2\mu \boldsymbol{I}_4$ with second- and forth-order identity tensors $\boldsymbol{I}_2$ and $\boldsymbol{I}_4$ and Lamé constants $\lambda = E\nu/[(1 + \nu)(1 - 2\nu)]$ and $\mu = E/[2(1 + \nu)]$

with given Young's modulus E and Poisson ratio ν describing isotropic material. The location $\boldsymbol{x}_{\max}$ is classified by

$$\mathcal{C}\left(\boldsymbol{x}_{\max}\right) = \begin{cases} \text{above perforation } P_k, & \text{if } \boldsymbol{x}_{\max} \text{ is associated and located above perforation } P_k, \\ \text{below perforation } P_k, & \text{if } \boldsymbol{x}_{\max} \text{ is associated and located below perforation } P_k. \end{cases} \tag{9}$$

Note that in the prescribed model the value of $F_{\max}$ is independend of the Young's modulus E and the Poisson ratio ν and linear proportional to the tensile strength f_{t}. The classifier $\mathcal{C}$ is always independend of E, ν and f_{t}, due to the constant structure.

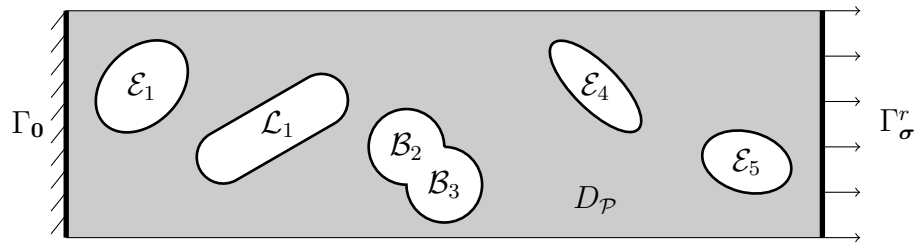

Figure 2: Schematical perforated domain and boundary conditions according to (3) and (8).

3 Experimental investigations

In the following the deterministic model type described in section 2 is investigated in an experimental setting based on various tensile tests, each leading to different outcome of failure behaviour.

3.1 Determination of material properties

For the experimental investigations of perforated structures, Plexiglas® – XT transparent – [5] is considered as isotropic material, described by Young's modulus E and Poisson ratio ν. Linear-elastic material behavior is assumed until the maximum first principal stress $\sigma_{1,\max}$ reaches the tensile strength f_{t}. Then, brittle behavior leads immediately to structural failure. In [5], the material parameters $E = 3300\mathrm{MN/m^2}$, $\nu = 0.37$ and $f_{\mathrm{t}} = 72\mathrm{MN/m^2}$ are given.

For verification, 15 specimens are manufactured and tested according to [2], see Figure 3. During the tensile testing, a force measurement system, optical extensometers and an optical strain field measurement system were used for measuring the applied force F, the integral axial strain ϵ_{g} and the continuous strain-field ϵ. With regard to defined standards in [2], the material properties are evaluated. As can be seen in Figure 4, present uncertainties lead to a scattering in the material parameters, especially in E. Nevertheless, the reference values for E and ν are validated and used in the following investigations within this contribution since the considered quantities of interest are invariant under E and ν, see Section 2. The discrepancy in the tensile strength f_{t} is even more important according to (7). Based on the conducted testing, a constant value of $f_{\mathrm{t}} = 64\mathrm{N/m^2}$ is assumed below.

3.2 Experimental failure analysis and deterministic numerical models

A perforated plate ($L \times W \times T = 150\mathrm{mm} \times 50\mathrm{mm} \times 4\mathrm{mm}$) is loaded by uniaxial tension to investigate the structural failure with the focus on the impact of the perforation properties. Ten specimens of

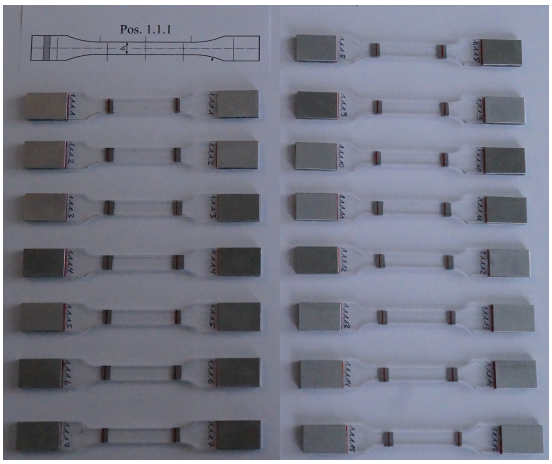

(a) Plexiglas® specimens goodfellow2016deep

(b) Uniaxial tensile testing

Figure 3: Determination of material properties according to [2]

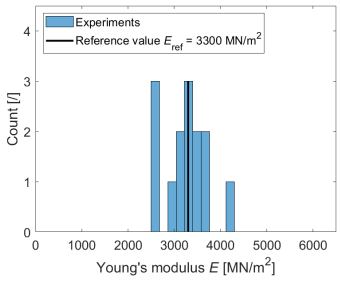

(a) Young's modulus E

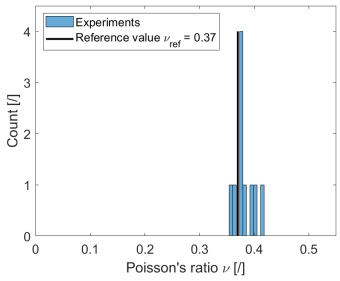

(b) Poisson ratio ν

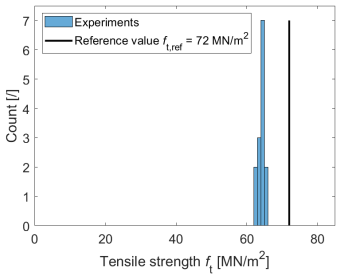

(c) Tensile strength f_{t}

Figure 4: Determined material properties

type 1 and 2 to be defined in Sections 3.2.1 and 3.2.2 were manufactured of the material described in Section 3.1 under equivalent conditions.

3.2.1 Specimen type 1

The domain $D_{\mathcal{P}}$ of specimen type 1 can be described mathematically as a rectangular plate D with constant thickness perforated by three circular holes $\mathcal{B}_i, i = 1 \dots 3$, with the values given in Table 2.

Table 2: Specimen type 1: Perforation parameters in $[\mathrm{mm}]$

perforation 1: $\mathcal{P}_1 = \mathcal{B}_1$	(x_1, y_1, d_1)	$=$	$(63, 40, 10)$
perforation 2: $\mathcal{P}_2 = \mathcal{B}_2$	(x_2, y_2, d_2)	$=$	$(69, 13, \ 8)$
perforation 3: $\mathcal{P}_3 = \mathcal{B}_3$	(x_3, y_3, d_3)	$=$	$(84, 32, 16)$

Figures 5a and 5b show the experimental setup and the specimen after testing with the associated ultimate load $F_{\max}$ and crack pattern that are called failure mechanism (FM).

As can be seen, the plates exhibit a scatter of ultimate loads $F_{\mathrm{exp},1} \in [2147\mathrm{N}, 2791\mathrm{N}]$ and various crack patterns, i.e. quantitative and qualitative differences of failure mechanism.

(a) Specimen type 1 before testing

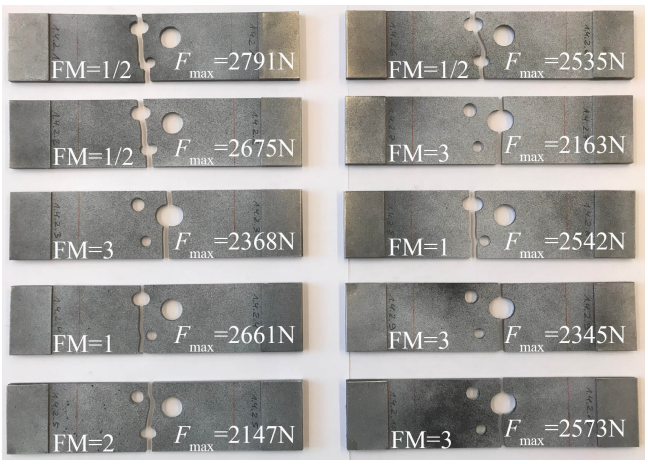

(b) Experimental results of specimen type 1

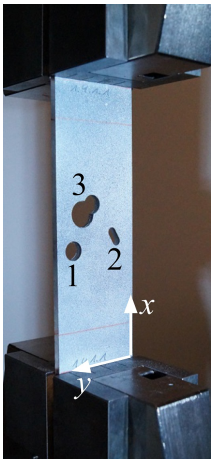

(c) Specimen type 2 before testing

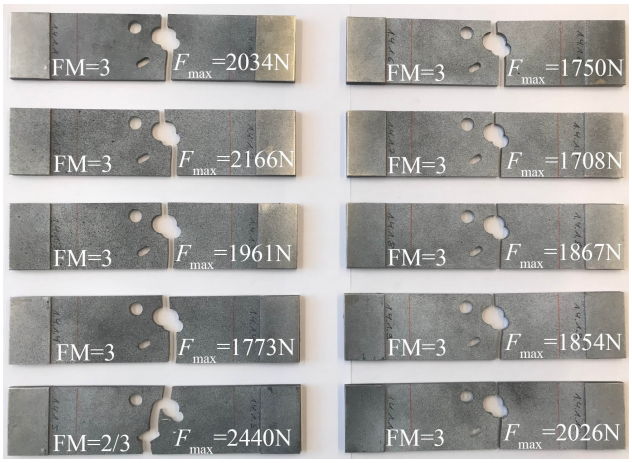

(d) Experimental results of specimen type 2

Figure 5: Specimen type 1 and 2 before and after testing

Analogously to the experiments in the numerical section, the left edge $\Gamma_{\mathbf{0}}$ is fixed and the right edge $\Gamma_{\boldsymbol{\sigma}}^{r}$ is loaded. The perforations are included as described in Section 2. The finite element model with boundary conditions in Figure 6a as well as the resulting first principal stresses in Figure 6b are displayed.

According to Table 3 the crack initiation $\boldsymbol{x}_{\max}$ is located at the maximum first principal stress $\sigma_{1,\max}$ above perforation 1 which leads to a failure mechanism 1 or $1/2$. Based on (7) with a tensile strength of $f_{\mathrm{t}} = 64\mathrm{MN}/\mathrm{m}^2$ from Section 3.1, the resulting ultimate load is computed to be $F_{\mathrm{det},1} = 2767\mathrm{N}$ in the deterministic case. Obviously, geometrical imperfections and experimental inaccuracies influence the ultimate load as well as the failure mechanism and therefore they have to be taken into account to investigate the structural failure in a realistic manner, see Section 5.

Table 3: Specimen type 1: Stress concentration factors $K_{\mathrm{tg}} = \lambda_{\max}(\boldsymbol{\sigma}(\boldsymbol{u}))/\sigma_{\mathrm{N}}$.

K_{tg}	location	K_{tg}	location
$\mathbf{4.626}$	**above perforation 1**	2.844	below perforation 1
4.062	above perforation 2	3.717	below perforation 2
3.755	above perforation 3	3.923	below perforation 3

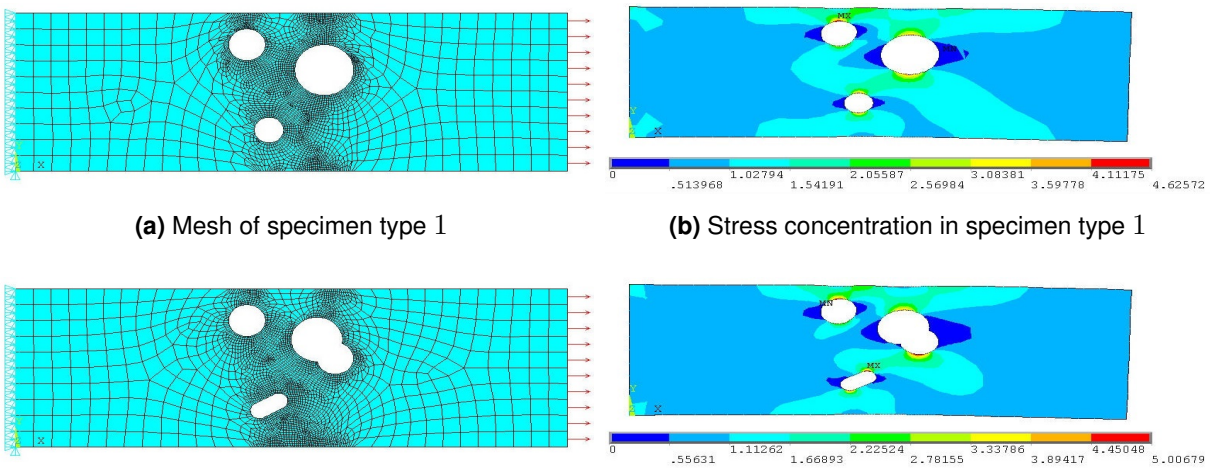

(a) Mesh of specimen type 1

(b) Stress concentration in specimen type 1

(c) Mesh of specimen type 2

(d) Stress concentration in specimen type 2

Figure 6: Deterministic numerical model of specimen type 1 and 2

3.2.2 Specimen type 2

Additionally to specimen type 1, a plate D perforated by three different types of holes was investigated. The perforations are given as follows: Perforation 1 is a circular hole $\mathcal{B}_1$, perforation 2 is a rotated slotted hole $\mathcal{L}_2$ and perforation 3 is an overlapping of two circular holes $\mathcal{B}_3 \cup \mathcal{B}_4$. Note that these types of perforations also fulfill the assumptions $(\mathbf{A1}) - (\mathbf{A3})$. The corresponding geometric parameters are given in Table 4. Figures 5c and 5d display again the experimental setup and the specimens after testing.

Table 4: Specimen type 2: Perforation parameters in $[\mathrm{mm}]$ or $[^\circ]$

perforation 1: $\mathcal{P}_1 = \mathcal{B}_1$	(x_1, y_1, d_1)	$=$	$(63, 40, 10)$
perforation 2: $\mathcal{P}_2 = \mathcal{L}_2$	$(x_2, y_2, l_2, w_2, \theta_2)$	$=$	$(69, 13, 11, \ 5, 30)$
perforation 3: $\mathcal{P}_3 = \mathcal{B}_3 \cup \mathcal{B}_4$	$(x_3, y_3, d_3, x_4, y_4, d_4)$	$=$	$(82, 34, 14, 87, 28, 10)$

The failure mechanisms of the ten specimens are very similar with a crack through perforation 3. Compared with specimen type 1, the ultimate loads are smaller and in a range of $F_{\mathrm{exp},2} \in [1708\mathrm{N}, 2440\mathrm{N}]$.

By contrast, the deterministic numerical model as shown in Figure 6d leads to a maximum stress concentration at perforation 2 with a resulting different crack growth. The associated ultimate load is computed to be $F_{\mathrm{det},2} = 2557\mathrm{N}$ which is greater than all experimental values. As a consequence the deterministic model is not able to explain the experimental outcome.

As can be seen in Table 5, the stress concentration factors are observed to be very close to each other at different locations. Consequently, the considered quantities of interest in (7) and (9) may be sensitive under slight changes of the present perforations. This assumption has to be validated within the uncertainty quantification approaches, see Sections 4 and 5.

4 Monomorphic and polymorphic uncertainty models

In order to explain the different outcomes of structural failure in the experiments of Section 3, this section sets its focus on modeling uncertainties of the underlying linear elastic model (3). The nature

Table 5: Specimen type 2: Stress concentration factors $K_{\mathrm{tg}} = \lambda_{\max}(\boldsymbol{\sigma}(\boldsymbol{u}))/\sigma_{\mathrm{N}}$

K_{tg}	location	K_{tg}	location
4.802	above perforation 1	2.805	below perforation 1
$\mathbf{5.007}$	**above perforation 2**	4.447	below perforation 2
4.195	above perforation 3	4.918	below perforation 3

of uncertainty arising for this problem alone can be arbitrarily complex, *e.g.* due to the fine scale shape of the Plexiglas® plate D, shape, location and size of perforations, material properties or description of source and force terms $\boldsymbol{f}$ and $\boldsymbol{h}$.

In what follows, the modelling of uncertainties is simplified and restricted to the location and size of perforations and the force term $\boldsymbol{h}$. The shape (slotted hole $\mathcal{L}$ / circular hole $\mathcal{B}$), material properties encoded in $\boldsymbol{C}$, the source term $\boldsymbol{f}$ and the unperforated domain D remain fixed.

Within this section two types of uncertainty models are considered. The *monomorphic* model includes probabilistic (stochastic) and possibilistic (in terms of fuzzy arithmetic) techniques and is discussed in section 4.1. The *polymorphic* uncertainty modeling is employed in the sense of a hybrid fuzzy-stochastic framework, see section 4.2.

Let $\boldsymbol{p}$ be an abstract parameter representing all uncertain input. Then there is a direct influence on the outcome of the maximum first principal stress (5) and the location classifier (9), both now depending on $\boldsymbol{p}$:

$$\boldsymbol{p} \mapsto \sigma_{1,\max}(\boldsymbol{p}) := \sigma_{1,\max}(\boldsymbol{u}_{\boldsymbol{p}}), \qquad \boldsymbol{p} \mapsto \mathcal{C}(\boldsymbol{p}) := \mathcal{C}(\boldsymbol{x}_{\max,\boldsymbol{p}}), \tag{10}$$

where $\boldsymbol{u}_{\boldsymbol{p}}$ and $\boldsymbol{x}_{\max,\boldsymbol{p}}$ denote the solution and the location of the maximum first principal stress for given $\boldsymbol{p} \in \bigtimes_{i=1}^{M}[a_i, b_i]$ for some $a_i, b_i \in \mathbb{R}$ and $M \in \mathbb{N}$. Note that the evaluation of the maps in (10) involves a computation of a (approximate) solution of the underlying elastic problem. In the uncertainty propagation this becomes the most expensive aspect and therefore it becomes necessary to construct surrogate maps. In our approach surrogates based on *Artifical Neural Networks* (ANNs) are constructed in Section 4.3.

4.1 Monomorphic uncertainty models

A common approach to model uncertainties is by means of a pure probabilistic or possibilistic formalism. Such an approach is called monomorphic uncertainty modeling. The following Sections 4.1.1 and 4.1.2 give a brief overview about both concepts.

4.1.1 Stochastic modeling

In this section a pure stochastic model in a randomly perforated domain is considered. Let $(\Omega, \Sigma, \mathbb{P})$ be a complete probability space [10]. Then for $\mathbb{P}$-*a.e.* $\omega \in \Omega$ let $D_{\mathcal{P}} = D_{\mathcal{P}}(\omega) := D \setminus \mathcal{P}(\omega)$, with $\mathcal{P}(\omega) := \{P_k(\omega) \in \mathcal{P} \colon k = 1, \dots, N_{\mathcal{P}}\}$ begin $\mathbb{P}$-a.e. of type $\mathcal{P}$ from (1). This is realized by letting the parameters (see Figure 1) of $P = P(\omega)$ be (possibly correlated) random variables.

- *Example:* Let $\mathcal{P} = \{\mathcal{B}_k(\omega), k = 1, \dots N_{\mathcal{P}}\}$ s.t. each ball $\mathcal{B}_k(\omega)$ is modeled by a random midpoint M_k and diameter d_k yielding a total random dimension $\dim = (1+d)N_{\mathcal{P}}$ with

$d = 2$. Hence, $\boldsymbol{p} \in \bigtimes_{k=1}^{N_{\mathcal{P}}} \operatorname{img} M_k \times \operatorname{img} d_k$ and a surrogate of the maps (10) has to be designed to tackle the curse of dimensionality.

For the present application the general random force field $\boldsymbol{h}$ in (8) is spatially constant modeled as

$$\boldsymbol{h}(\boldsymbol{x}, \omega) := Q[\alpha_{\mathrm{F}}(\omega)]\boldsymbol{e}_1, \quad \boldsymbol{x} \in \Gamma^r_{\boldsymbol{\sigma}}, \tag{11}$$

with a random variable $\alpha_{\mathrm{F}} \colon \Omega \mapsto \mathbb{R}$ with $\operatorname{img} \alpha_{\mathrm{F}}(\Omega) \subset [0, 2\pi)$. For the sake of simplicity the material tensor $\boldsymbol{C}$ and the source term $\boldsymbol{f}$ remain non-random and constant. In this situation, $\sigma_{1,\max} = \sigma_{1,\max}(\omega)$ and $\mathcal{C} = \mathcal{C}(\omega)$ from (10) become random variables. A prominent type of random variables ξ follows a uniform distribution $\mathcal{U}(a; b)$, in short $\xi \sim \mathcal{U}(a; b)$ for $a, b \in \mathbb{R}, a < b$. For numerical experiments, a perforation P_k is parametrized with $\boldsymbol{\xi} = (\xi)$ with independent $\xi \sim \mathcal{U}(a; b)$, s.t. $P_k(\omega) = P_k(\boldsymbol{\xi}(\omega))$.

4.1.2 Fuzzy modeling

In this section a pure possibilistic model is presented in terms of fuzzy arithmetic [22, 15, 13]. Let $Z \subset \mathbb{R}^M$ be a non-empty set and consider a map

$$\mu_{\tilde{z}} \colon Z \mapsto [0, 1] \tag{12}$$

called a (joint) membership function on Z describing a fuzzy set

$$\tilde{z} := \{(z, \mu_{\tilde{z}}(z)) \colon z \in Z\}. \tag{13}$$

Moreover, if Z is bounded and convex, $\mu_{\tilde{z}}$ is quasi-concave and upper semi-continuous and, additionally, there is a unique $z^* \in Z$ with $\mu_{\tilde{z}}(z^*) = 1$, then $\tilde{z}$ is called a fuzzy vector for $M > 1$ or a fuzzy number for $M = 1$. Denote by $\mathcal{F}(Z)$ the set of all fuzzy vectors/numbers on Z and write $\mathcal{Z} \in \mathcal{F}(Z)$. A special case is the non-interactive setting of a fuzzy vector $\tilde{z}$: Let $\tilde{z}_i \in \mathcal{F}(Z_i)$ with $Z_i \subset \mathbb{R}$ for $i = 1, \ldots, M > 1$ and a fuzzy set $\tilde{z} = (\tilde{z}_1, \ldots, \tilde{z}_M)$ given with a joint membership function of the form

$$\mu_{\tilde{z}}(\boldsymbol{z}) = \min_{i=1,\ldots,M} \mu_{\tilde{z}_i}(z_i), \quad z = (z_1, \ldots, z_M) \in Z := \bigtimes_{i=1}^{M} Z_i. \tag{14}$$

Then the fuzzy vector $\tilde{z}$ is called *non-interactive* according to ZADEH [22]. The propagation of fuzzy vectors/numbers through maps is defined by means of the *extension principle*: Let $f \colon Z \mapsto V$ be a function and $\tilde{z}$ be a fuzzy set on Z, then $\tilde{v} := f(\tilde{z})$ defines a fuzzy set on V with membership function $\mu_{\tilde{v}}$ defined as

$$\mu_{\tilde{v}}(v) := \begin{cases} \sup_{f(z)=v} \mu_Z(z), & f^{-1}(v) \neq \emptyset, \\ 0, & f^{-1}(v) = \emptyset. \end{cases} \tag{15}$$

Moreover if f is continuous and $V \subset \mathbb{R}$, the fuzzy propagation may be characterized via constrained optimization on α-cuts due to a function-set identity [16] on compact sets. Let $C_\alpha[\tilde{z}] := \{z \in Z \colon \mu_{\tilde{z}}(z) \geq \alpha\}$ for $\alpha \in [0, 1]$ denote the α-cut of a fuzzy set $\tilde{z}$ and $C_\alpha[\tilde{v}]$ the α-cut of $\tilde{v}$, then it holds

$$C_\alpha[\tilde{v}] = \left[\min_{z \in C_\alpha[\tilde{z}]} f(z), \max_{z \in C_\alpha[\tilde{z}]} f(z) \right]. \tag{16}$$

The most prominent example of a fuzzy set is the so called triangular fuzzy number

$$\tilde{z} = \langle l; z^*; r \rangle, \quad -\infty < l < z^* < r < \infty, \tag{17}$$

for a fuzzy number described by a triangular membership function, see Figure 7. The optimization required due to the extension principle (15) may become a complicated task in computations. Thus *three* main concepts to realize the propagation are considered:

- *Semi sampling in* V: Directly solve the constrained optimization problem with a global optimizer. For a given sequence $(v_k)_k \subset V$, compute the supremum over $Z_k := \{z \in Z : f(z) = v_k\}$, see red line in Figure 7.

- *Full sampling approach*: Choose a sequence $(z_k)_k \subset Z$ and compute $(f_k)_k = [f(z_k)]_k$ and $(\mu_k)_k = [\mu_{\tilde{z}}(z_k)]_k$. Use the data sample pairs (v_k, μ_k) and reconstruct $\mu_{\tilde{f}}$, *e.g.* by convex hull or an envelope approach, see orange/purple graphics in Figure 7.

- α*-cut optimization*: Based on (16) with $V = \mathbb{R}$ for a given discretization $\alpha \in \{\alpha_1, \dots, \alpha_l\} \subset [0, 1]$, compute $C_\alpha[\tilde{f}]$ and build $\mu_{\tilde{f}}$ based on interpolation between the obtained points, see blue graphics in Figure 7.

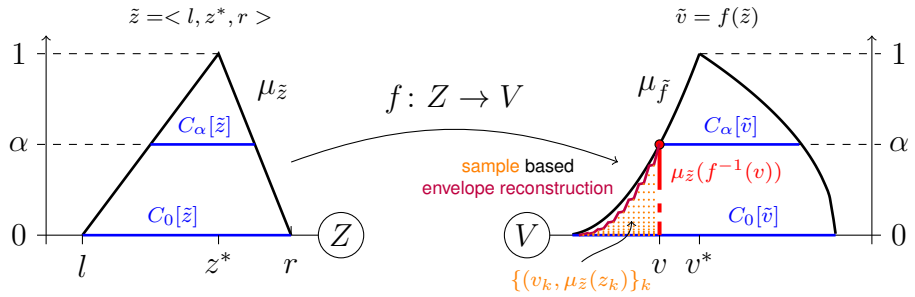

Figure 7: Fuzzy propagation via α-cuts or full-sampling and membership reconstruction with $v_k = f(z_k)$, for $Z = V = \mathbb{R}$.

Within the uncertainty parametrization in a possibilistic framework, all parameters describing the perforations and the force term direction α_{F} as in (11) are modeled as triangular fuzzy numbers, all other parameters remain deterministic.

4.2 Polymorphic uncertainty model

The modeling with both stochastic (probabilistic) and fuzzy (possibilistic) dependency is denoted as polymorphic uncertainty modeling. By what follows assume a parametric description by a parameter $\boldsymbol{p}$ of the uncertain model motivated by the quantities of interests considered in (10). In this setting, the dependency of a random variable $\boldsymbol{\xi}$ and a fuzzy variable $\tilde{z}$ may be divided into two cases [3]:

- *Separated dependence*: $\boldsymbol{p} = (\boldsymbol{\xi}, \tilde{z})$ with a random vector $\boldsymbol{\xi}$ and a fuzzy set $\tilde{z}$.

- *Coupled dependence*: $\boldsymbol{p} = \boldsymbol{\xi}(\tilde{z})$ with a random vector $\boldsymbol{\xi}$ depending on fuzzy input.

The latter structure may occur, when random variables follow a distribution defined by parameters that are fuzzy variables [7, 17], *e.g.* mean and variance for a normal distribution. Both cases are abbreviated by the notation $\boldsymbol{p} = \boldsymbol{p}(\boldsymbol{\xi}, \tilde{z})$. While the propagation for both structures can be carried out similarly, possible underlying surrogates may be adapted with the coupled or separated parameter structure itself, *e.g.* with tensor-based surrogates for the latter case.

In the separated case, let $\Xi := \operatorname{img} \boldsymbol{\xi}$ and recall the notation Z to be the underlying domain of the fuzzy variable $\tilde{z}$. For a set V consider a measurable map

$$f \colon \Xi \times Z \mapsto V, \quad (y, z) \mapsto f(y, z). \tag{18}$$

Then, $\tilde{v}(\omega) := f(\boldsymbol{\xi}(\omega), \tilde{z})$ is a random fuzzy set in V denoted as *polymorphic field*: For $\mathbb{P}$-*a.e.* $\omega \in \Omega$

$$\mu_{\tilde{v}(\omega)}(\boldsymbol{\xi}(\omega); \cdot) \colon V \mapsto [0, 1], \quad v \mapsto \mu_{\tilde{v}(\omega)}(\boldsymbol{\xi}(\omega); v), \tag{19}$$

indexed by $\boldsymbol{\xi}(\omega)$ defines a membership of $\tilde{v}(\omega) \in \mathcal{F}(V)$ via ZADEH's extension principle, see (15). Thus, on the one hand, the membership function itself is a random field

$$\mu_Y \colon \Omega \times Y \mapsto [0, 1]. \tag{20}$$

On the other hand, for fixed $z \in Z$, $\omega \to f(\boldsymbol{\xi}(\omega), z)$ is a random variable. An abstract propagation concept of polymorphic input is summarized in Algorithm 1.

Algorithm 1: Abstract uncertainty propagation of polymorphic uncertainty

input : ∘ parameter $\boldsymbol{p} = \boldsymbol{p}(\boldsymbol{\xi}, \tilde{z})$, random vector $\boldsymbol{\xi}$, fuzzy input $\tilde{z}$ with membership function $\mu_{\tilde{z}}$
∘ point evaluation selection strategy in fuzzy space $\mathcal{A}_{\mathcal{F}}$
∘ point evaluation selection strategy in stoch. space $\mathcal{A}_{\Omega}$
∘ polymorph uncertainty model $\mathcal{M} = \mathcal{M}(\boldsymbol{p})$ with values in Y

output: discrete data set of V-valued polymorphic field $\tilde{v} := f(\mathcal{M})$

1 collect evaluation points based on $\mathcal{A}_{\mathcal{F}}$ into $\mathcal{F} := \{z_i \in Z, z_i \in \operatorname{supp} \mu_Z, i = 1, \dots, N_{\mathcal{F}} < \infty\}$
2 collect evaluation points based on $\mathcal{A}_{\Omega}$ into $\mathcal{S} := \{\boldsymbol{\xi}_k, k = 1, \dots, N_{\mathcal{S}} < \infty\}$
3 **foreach** $\boldsymbol{\xi}_k \in \mathcal{S}$ **do**
4 reconstruct $\mu_Y(\boldsymbol{\xi}_k, \cdot)$ based on (15) via evaluation of $f_Z \colon Z \mapsto Y, f_k(z) = f(\boldsymbol{p}(\boldsymbol{\xi}_k, z))$ on $\mathcal{A}_{\mathcal{F}}$
5 define fuzzy set $\tilde{v}_k := \{(f_k(z), \mu_{\tilde{v}_k}(\boldsymbol{\xi}_k, f_k(z))) \colon z \in Z\}$

return discrete fuzzy set data $\{\tilde{v}_k, k = 1, \dots, N_{\mathcal{S}}\}$.

Note that the selection strategies $\mathcal{A}_{\mathcal{F}}$ and $\mathcal{A}_{\Omega}$ are rather abstract and may depend on one another.

For the stochastic coordinate space, $\mathcal{A}_{\Omega}$ may be chosen as interpolation or quadrature possibly used for functional representations (sparse grid interpolation, generalized polynomial chaos) or any sampling scheme involving Monte-Carlo or quasi Monte-Carlo simulation for stochastic coordinates.

The strategy for the fuzzy coordinate may be chosen based on iterations of an underlying min/max optimization routine within an α-cut discretization. Recall that for the latter case to be possible, the map f_k needs to be continuous and $V = \mathbb{R}$. In the special case that f_k from Algorithm 1 is continuous and monotone, the propagation of fuzzy input further simplifies as the optimization problem (16) becomes simpler. This observation is intensively used in the numerical examples in Section 5.2. In the general case of f_k, sampling approaches directly based on (15) and reconstruction of the output membership functions may be considered, see Section 4.1.2 and Figure 7.

In Algorithm 1 it is assumed that one is interested in a polymorphic field $\tilde{v}$. In practise often only statistics of f are relevant, *e.g.* moments $\mathbb{E}[f^m]$ for some $m \in \mathbb{N}$. In this case, a partial stochastic propagation can be performed leading to (deterministic) fuzzy outputs.

Within the framework of considered quantities of interests, the maximum first principal stress and the classifier in (10) are now fuzzy-stochastic outcomes, *i.e.* random variables that depend on fuzzy input as well. The parameters describing the size of the perforations are modeled with triangular fuzzy numbers, the remaining parameters are random variables. A separated dependence is considered with non-interactive fuzzy numbers and mutual independent random variables.

4.3 Surrogates based on ANNs

In the last sections the need of surrogates for the map $f\colon \Xi \times Z \to V$ was emphasized, assuming that each evaluation of f is expensive. In this work Artifial Neural Networks (ANNs) are chosen as a particular type of surrogate. The successful application of ANNs and its variants like Convolutional Neural Networks for image classification, *e.g.* [11], and Recurrent Neural Networks for audio recognition [6] has been demonstrated extensively in the literature. Among the vast of literature, it is only refered to [6] and references therein for a broader overview.

In this work, regression based classical feed forward Neural Networks are considered for predicting both the maximum first principal stress $\boldsymbol{p} \mapsto \sigma_{1,\max}(\boldsymbol{p})$ and the location classifier $\boldsymbol{p} \mapsto \mathcal{C}(\boldsymbol{p})$ from (10). Any presented ANN is realized with the open source software Keras [1]. These network structures yield promising results as demonstrated in Section 5. In Figure 8 the used network topology is illustrated, consisting of an input an output layer as well as hidden layers denoted as

$$\mathcal{H} = \mathcal{H}(\boldsymbol{n}), \quad \boldsymbol{n} = (n_1, \dots, n_H) \in \mathbb{N}^H, \tag{21}$$

consisting of $H \in \mathbb{N}$ layers and $n_k \in \mathbb{N}$ denoting the number of neurons in the k-th hidden layer for $k = 1, \dots, H$, and an output layer. For the maximum first principal stress map $\boldsymbol{p} \mapsto \sigma_{1,\max}(\boldsymbol{p})$, an ELU activation function is considered, see red path in Figure 8 and the parameters W_ℓ^1, $\ell = 0, \dots, L$ of the ANN are trained by minimizing mean square error (MSE) functional, given a set of training samples. The classifier map $\boldsymbol{p} \mapsto \mathcal{C}(\boldsymbol{p})$ will be approximated using RELU activation functions and a softmax activation on the output layer, see blue path in Figure 8. For the classification minimizing a categorial cross entropy (CE) loss is used to fit the parameters W_ℓ^2 in the ANN for $\ell = 0, \dots, L = H + 1$.

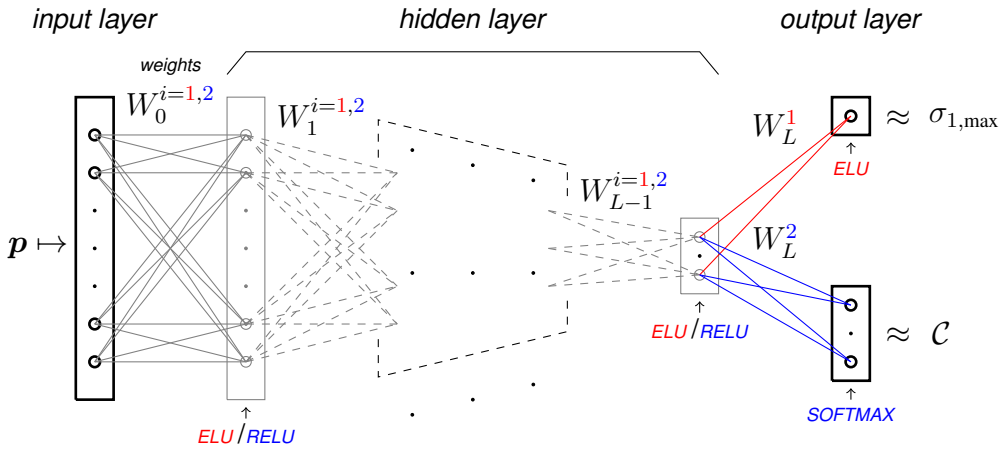

Figure 8: Schematical dense feed forward network used as surrogate in Section 5 with decreasing number of neurons inside the hidden layers.

Let $\boldsymbol{p} \in \mathbb{R}^d$. Then all considered dense feed-forward structures are chosen, s.t. the first hidden layer contains $n_1 = d$ neurons. This is motivated by the idea that the ANN is able to reorder the input

parameters in a non-linear manner to improve the approximation quality. Successively each follow up hidden layer consists of a not larger number of neurons, *i.e.* $n_1 \geq n_2 \geq \ldots \geq n_H$. Details on the explicit construction and training for the present application are given below.

The following subsections briefly describe the training and validation process of the involved ANNs each based on $N = 10000 = 7500 + 2500 = N_{\text{train}} + N_{\text{test}}$ uniform distributed samples within the parameter range, see Table 6 for specimen type 1 and Table 7 for specimen type 2, respectively. An Adams optimization scheme is used for all involved ANNs with a learning rate of 0.001. In the optimization routine a model checkpoint based on a *save best* strategy with a patience of 50 iterations is used for the resulting surrogate ANNs.

4.3.1 Specimen type 1

The uncertainity model of specimen type 1 involves a total of 10 parameters. The surrogate ANN structure for the maximum principal stress is specified by $\mathcal{H}(\boldsymbol{n})$ with $\boldsymbol{n} = (10, 8, 6, 4, 4, 2)$ and ELU activation per layer. The model is trained in a sequence of batches/epochs of $(20, 300) \rightarrow (50, 1000)$, resulting in about 1% training loss and 2% validation loss. The overall sample data consists of 4 classes $(\mathrm{A1}, \mathrm{A2}, \mathrm{B2}, \mathrm{A3})$, see Figure 9 for illustration. The classifier ANNs topology consists of $\boldsymbol{n} = (10, 8, 6, 4)$ with RELU activation and softmax output layer. It is trained with class weight of $w = (1, 1.2, 1.1, 1)$ using a sequence of batches/epochs of $(150, 5) \rightarrow (120, 40) \rightarrow (120, 100) \rightarrow (150, 200)$. Within the optimization a training loss of 2% and 97% validation accucary was archieved.

4.3.2 Specimen type 2

The uncertainity model of specimen type 2 involves a total of 15 parameters. The surrogate ANN structure for the maximum principal stress is specified by $\mathcal{H}(\boldsymbol{n})$ with $\boldsymbol{n} = (15, 10, 8, 6, 2)$ and ELU activation per layer. The model is trained in a sequence of batches/epochs of $(20, 300) \rightarrow (50, 400)$, resulting in about 2% training loss and 3% validation loss. The overall sample data consists of 4 classes $(\mathrm{A1}, \mathrm{A2}, \mathrm{B2}, \mathrm{A3}, \mathrm{B3})$, see Figure 10 for illustration. The classifier ANNs topology consists of $\boldsymbol{n} = (15, 8, 6, 4)$ with RELU activation and softmax output layer. It is trained with equals class weights using a sequence of batches/epochs of $(20, 5) \rightarrow (40, 40) \rightarrow (100, 100) \rightarrow (150, 200)$. Within the optimization a training loss of 1.8% and 96% validation accucary was archieved.

5 Comparison of different uncertainty quantification approaches with experimental investigations

Regarding the experimental investigations of perforated structures described in Section 3.2, uncertainties are identified during the fabrication and the experiments. Manufacturing inaccuracies and imperfections influence the locations and sizes of the perforations while the experimental conditions lead to a scattering load angle. In the following, the same ranges for the uncertain parameters are used independently of the uncertainty quantification approach formulated in Section 4.

5.1 Monomorphic uncertainty models

In the presented experiments, the deterministic model from Section 2 is enriched by a monomorphic description of geometric and load angle parameters for both specimens.

5.1.1 Stochastic modeling

For the probabilistic approach, the described uncertainties are quantified by uniform distributed stochastically independent variables, see Table 6 for specimen type 1 and Table 7 for specimen type 2, respectively.

Table 6: Specimen type 1: stochastic variables in $[\mathrm{mm}]$ or $[^\circ]$

$\mathcal{P}_1 = \mathcal{B}_1$	$\mathcal{P}_2 = \mathcal{B}_2$	$\mathcal{P}_3 = \mathcal{B}_3$	load angle
$x_1 \sim \mathcal{U}(61; 65)$	$x_2 \sim \mathcal{U}(67; 71)$	$x_3 \sim \mathcal{U}(82; 86)$	$\alpha_{\mathrm{F}} \sim \mathcal{U}(-2; 2)$
$y_1 \sim \mathcal{U}(38; 42)$	$y_2 \sim \mathcal{U}(11; 15)$	$y_3 \sim \mathcal{U}(30; 34)$	
$d_1 \sim \mathcal{U}(9.5; 10.5)$	$d_2 \sim \mathcal{U}(7.5; 8.5)$	$d_3 \sim \mathcal{U}(15.5; 16.5)$	

Table 7: Specimen type 2: stochastic variables in $[\mathrm{mm}]$ or $[^\circ]$

$\mathcal{P}_1 = \mathcal{B}_1$	$\mathcal{P}_2 = \mathcal{L}_2$	$\mathcal{P}_3 = \mathcal{B}_3 \cup \mathcal{B}_4$	load angle
$x_1 \sim \mathcal{U}(61; 65)$	$x_2 \sim \mathcal{U}(67; 71)$	$x_3 \sim \mathcal{U}(80; 84)$	$\alpha_{\mathrm{F}} \sim \mathcal{U}(-2; 2)$
$y_1 \sim \mathcal{U}(38; 42)$	$y_2 \sim \mathcal{U}(11; 15)$	$y_3 \sim \mathcal{U}(32; 36)$	
$d_1 \sim \mathcal{U}(9.5; 10.5)$	$l_2 \sim \mathcal{U}(9; 13)$	$d_3 \sim \mathcal{U}(13.5; 14.5)$	
	$w_2 \sim \mathcal{U}(4.5; 5.5)$	$x_4 \sim \mathcal{U}(85; 89)$	
	$\theta_2 \sim \mathcal{U}(28; 32)$	$y_4 \sim \mathcal{U}(26; 30)$	
		$d_4 \sim \mathcal{U}(9.5; 10.5)$	

By applying a classical Monte Carlo sampling approach with $N = 10^4$ direct model problem simulations and $N = 10^6$ surrogate forcasts obtained from the trained ANNs, the numerical outputs for specimen type 1 in Figure 9 and for specimen type 2 in Figure 10 are obtained.

For both specimen types, the numerical results cover the range of experimental ones even though a shift is recognizable. The peak is on the right of the experimental range, leading to the conclusion that some other uncertainties have to be taken into account additionally which reduce the ultimate load $F_{\max}$. However, the empirical mean is located inside the experimental range and different locations of the maximum first principal stress occurs in the numerical simulations, like it has been assumed due to the different crack patterns in the experimental investigations. The stochastic output arised from the classical sampling approach and the surrogate modeling are qualitatively as well as quantitatively quite similar. The deviation of the empirical mean is less than 1% for both specimens. A benefit of this approach is the direct visibility of partial probabilities of different locations of the maximum first principal stress, e.g. within a certain range of ultimate loads.

For specimen type 1, the maximum stress location *above perforation* 1 is most probable and is represented over the whole range of the ultimate load. The location *above* or *below perforation* 2 depends mainly on the distance to the other perforations as well as to the lower edge and is represented for higher values of $F_{\max}$. The location *above perforation* 3 is least probable and also related to higher ultimate loads caused by larger edge distance even if perforation 3 is the largest. Within the numerical simulations, the maximum first principal stress was not located either *below perforation* 1 or 3.

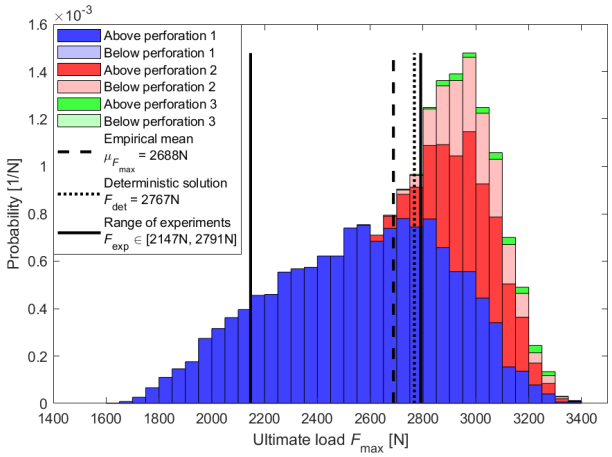

(a) Empirical distribution (sampling approach)

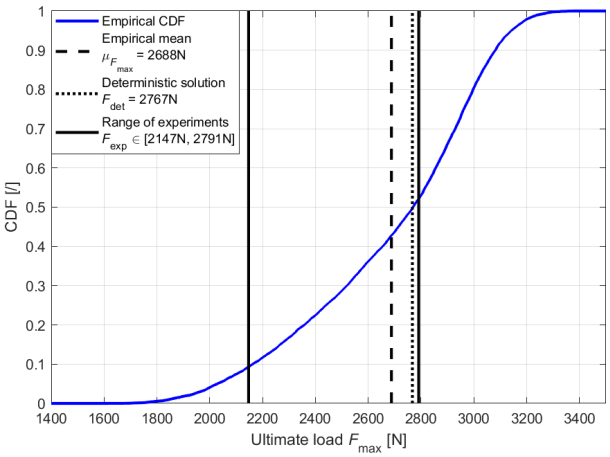

(b) CDF (sampling approach)

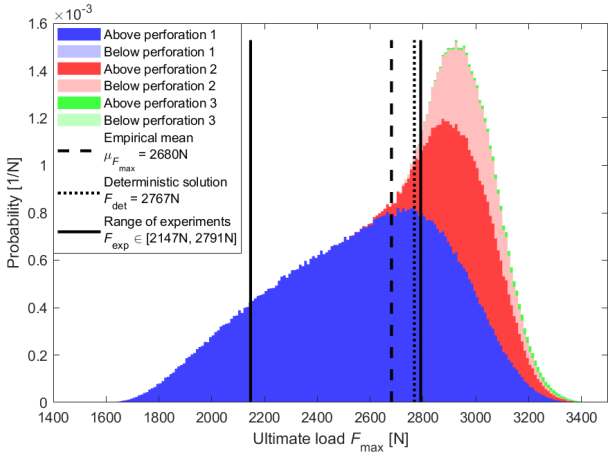

(c) Empirical distribution (surrogate modeling)

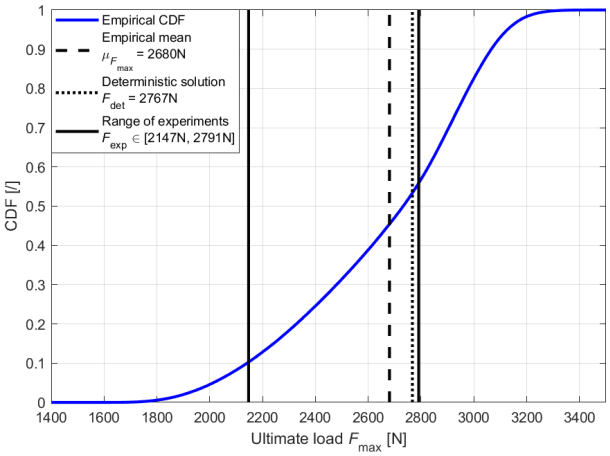

(d) CDF (surrogate modeling)

Figure 9: Stochastic output for specimen type 1.

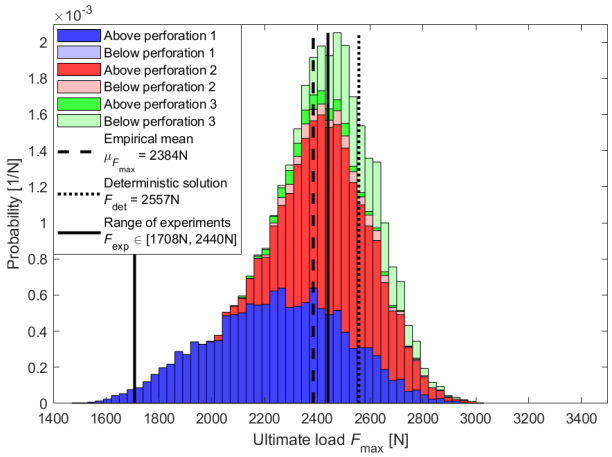

(a) Empirical distribution (sampling approach)

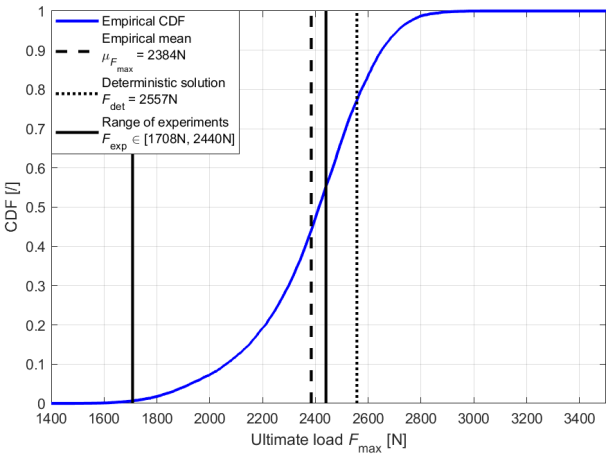

(b) CDF (sampling approach)

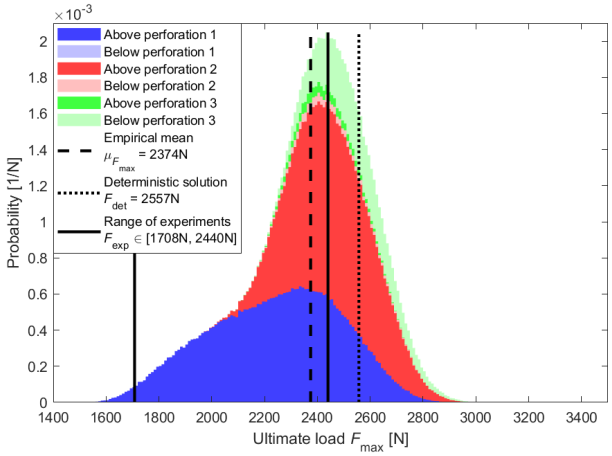

(c) Empirical distribution (surrogate modeling)

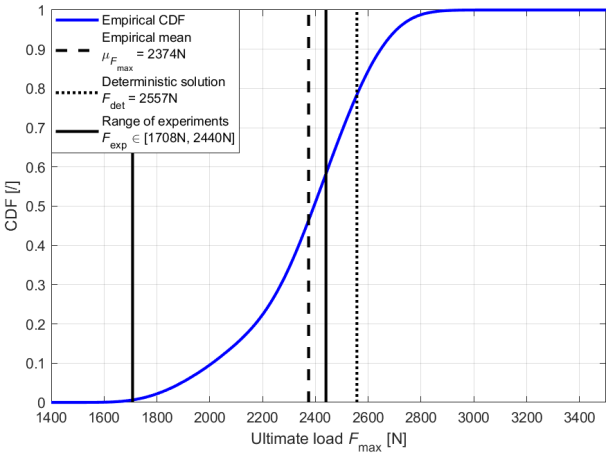

(d) CDF (surrogate modeling)

Figure 10: Stochastic output for specimen type 2.

For specimen type 2, all locations except the ones *below perforation* 1 are reproducible. The locations associated to perforation 2 and 3 are more represented compared to specimen type 1 and related to lower ultimate loads. The location *above perforation* 1 is again visible over the whole range of $F_{\max}$, however, for higher values, a location associated to perforation 2 or 3 is more probable.

5.1.2 Fuzzy modeling

In the possibilistic approach, the described uncertainties are quantified by independent triangular fuzzy numbers, see Table 8 for specimen type 1 and Table 9 for specimen type 2, respectively.

Table 8: Specimen type 1: fuzzy numbers in $[\mathrm{mm}]$ or $[^\circ]$

$\mathcal{P}_1 = \mathcal{B}_1$	$\mathcal{P}_2 = \mathcal{B}_2$	$\mathcal{P}_3 = \mathcal{B}_3$	load angle
$x_1 = \langle 61; 63; 65\rangle$	$x_2 = \langle 67; 69; 71\rangle$	$x_3 = \langle 82; 84; 86\rangle$	$\alpha_{\mathrm{F}} = \langle -2; 0; 2\rangle$
$y_1 = \langle 38; 40; 42\rangle$	$y_2 = \langle 11; 13; 15\rangle$	$y_3 = \langle 30; 32; 34\rangle$	
$d_1 = \langle 9.5; 10; 10.5\rangle$	$d_2 = \langle 7.5; 8; 8.5\rangle$	$d_3 = \langle 15.5; 16; 16.5\rangle$	

Table 9: Specimen type 2: fuzzy numbers in $[\mathrm{mm}]$ or $[^\circ]$

$\mathcal{P}_1 = \mathcal{B}_1$	$\mathcal{P}_2 = \mathcal{L}_2$	$\mathcal{P}_3 = \mathcal{B}_3 \cup \mathcal{B}_4$	load angle
$x_1 = \langle 61; 63; 65\rangle$	$x_2 = \langle 67; 69; 71\rangle$	$x_3 = \langle 80; 82; 84\rangle$	$\alpha_{\mathrm{F}} = \langle -2; 0; 2\rangle$
$y_1 = \langle 38; 40; 42\rangle$	$y_2 = \langle 11; 13; 15\rangle$	$y_3 = \langle 32; 34; 36\rangle$	
$d_1 = \langle 9.5; 10; 10.5\rangle$	$l_2 = \langle 9; 11; 13\rangle$	$d_3 = \langle 13.5; 14; 14.5\rangle$	
	$w_2 = \langle 4.5; 5; 5.5\rangle$	$x_4 = \langle 85; 87; 89\rangle$	
	$\theta_2 = \langle 28; 30; 32\rangle$	$y_4 = \langle 26; 28; 30\rangle$	
		$d_4 = \langle 9.5; 10; 10.5\rangle$	

In this approach, a classical sampling approach with $n = 10^4$ simulations is also compared to a surrogate model with $n = 10^6$ simulations in total. In addition to the deterministic case on the core for $\mu = 1.0$, ten equidistantly distributed α-cuts are used to ensure a homogeneous distribution of the samples over the height of the membership function. The numerical outputs are displayed for specimen type 1 in Figure 11 and for specimen type 2 in Figure 12, respectively.

As in the probabilistic approach, the experimental range is completely covered by the numerical results despite the shift to the left side. The core of the output membership function represents the deterministic solution which is for specimen type 1 at the upper bound and for specimen type 2 outside of the experimental range. Also, 4 resp. 5 different locations of the maximum first principal stress are recognizable in the numerical simulations. The output membership function is tilted to lower ultimate loads $F_{\max}$ even though all input membership functions are symmetrical triangular fuzzy numbers. Comparing the output of the sampling approach with the surrogate solution, a good agreement of the membership functions as well as of the different locations is shown whereby the surrogate modeling lead to a higher range of ultimate loads, e.g. visible in the support of $F_{\max}$. Furthermore, the possibilities of the different locations depend on the output membership function value, thus they can be related to the range of input uncertainties, which is an added value of this pure fuzzy approach.

For specimen type 1, small input uncertainties lead to a stress concentration *above perforation* 1 since it is represented over the entire height of the membership function. With increasing input uncertainties, also the locations *above perforation* 2, *below perforation* 2 and *above perforation* 3 successively become possible, mainly related to higher ultimate loads $F_{\max}$.

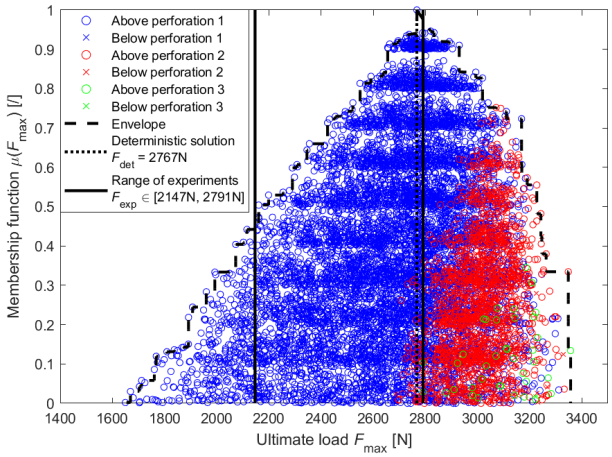

(a) Empirical membership function (sampling approach)

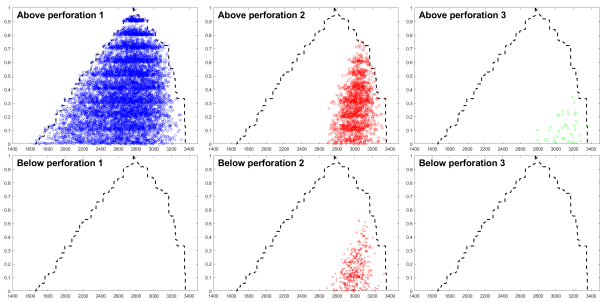

(b) Individual components (sampling approach)

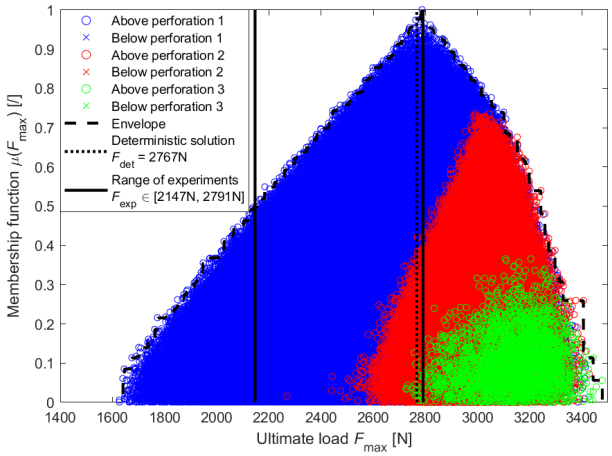

(c) Empirical membership function (surrogate modeling)

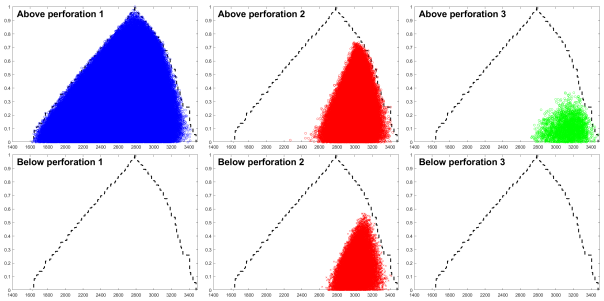

(d) Individual components (surrogate modeling)

Figure 11: Fuzzy output for specimen type 1

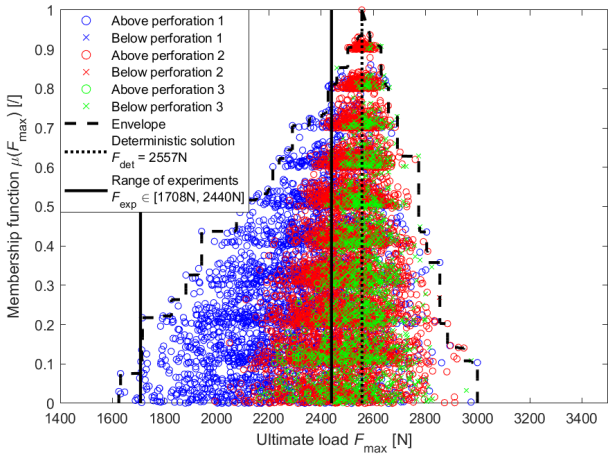

(a) Empirical membership function (sampling approach)

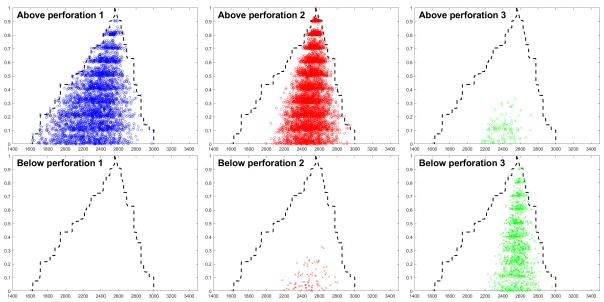

(b) Individual components (sampling approach)

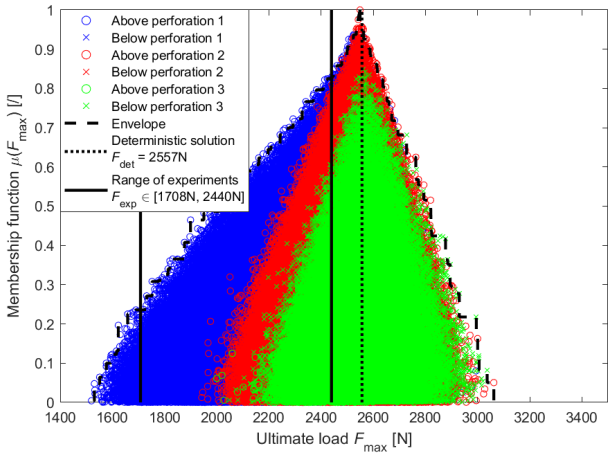

(c) Empirical membership function (surrogate modeling)

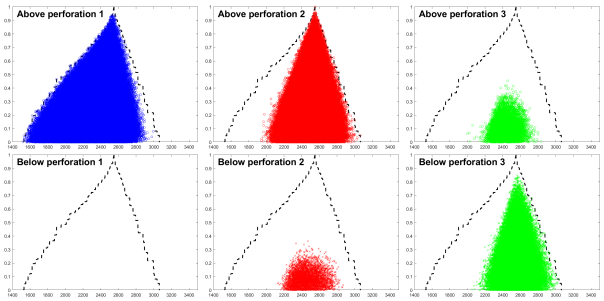

(d) Individual components (surrogate modeling)

Figure 12: Fuzzy output for specimen type 2

For specimen type 2, the locations *above perforation* 1, *above perforation* 2 and *below perforation* 3 appear almost over the entire height of the membership function independently of the input uncertainty ranges. While lower valued ultimate loads are mainly caused by the first perforator 1 the two other perforations are more represented for higher values. Consequently for small input uncertainties and consequently higher output membership function values, a stress concentration *below perforation* 2 or *above perforation* 3 is not expected.

5.2 Polymorphic uncertainty model

In a polymorphic approach, stochastic and fuzzy variables are applied simultaneously. As an example, the described uncertainties except the size parameters are described by uniformly distributed stochastically independent variables like in Section 5.1.1, whereas independent triangular fuzzy numbers are used for the size parameters like in Section 5.1.2, see Table 10 for specimen type 1 and Table 11 for specimen type 2, respectively.

Table 10: Specimen type 1: stochastic and fuzzy variables in $[\mathrm{mm}]$ or $[^\circ]$

$\mathcal{P}_1 = \mathcal{B}_1$	$\mathcal{P}_2 = \mathcal{B}_2$	$\mathcal{P}_3 = \mathcal{B}_3$	load angle
$x_1 \sim \mathcal{U}(61; 65)$	$x_2 \sim \mathcal{U}(67; 71)$	$x_3 \sim \mathcal{U}(82; 86)$	$\alpha_\mathrm{F} \sim \mathcal{U}(-2; 2)$
$y_1 \sim \mathcal{U}(38; 42)$	$y_2 \sim \mathcal{U}(11; 15)$	$y_3 \sim \mathcal{U}(30; 34)$	
$d_1 = \langle 9.5; 10; 10.5\rangle$	$d_2 = \langle 7.5; 8; 8.5\rangle$	$d_3 = \langle 15.5; 16; 16.5\rangle$	

Table 11: Specimen type 2: stochastic and fuzzy variables in $[\mathrm{mm}]$ or $[^\circ]$.

$\mathcal{P}_1 = \mathcal{B}_1$	$\mathcal{P}_2 = \mathcal{L}_2$	$\mathcal{P}_3 = \mathcal{B}_3 \cup \mathcal{B}_4$	load angle
$x_1 \sim \mathcal{U}(61; 65)$	$x_2 \sim \mathcal{U}(67; 71)$	$x_3 \sim \mathcal{U}(80; 84)$	$\alpha_\mathrm{F} \sim \mathcal{U}(-2; 2)$
$y_1 \sim \mathcal{U}(38; 42)$	$y_2 \sim \mathcal{U}(11; 15)$	$y_3 \sim \mathcal{U}(32; 36)$	
$d_1 = \langle 9.5; 10; 10.5\rangle$	$l_2 = \langle 9; 11; 13\rangle$	$d_3 = \langle 13.5; 14; 14.5\rangle$	
	$w_2 = \langle 4.5; 5; 5.5\rangle$	$x_4 \sim \mathcal{U}(85; 89)$	
	$\theta_2 \sim \mathcal{U}(28; 32)$	$y_4 \sim \mathcal{U}(26; 30)$	
		$d_4 = \langle 9.5; 10; 10.5\rangle$	

Monotony of F_max with regard to the size parameters is presumed which enables the reduced transformation method [8] for the analysis in the fuzzy space. For the stochastic parameters, a classical Monte-Carlo sampling approach with $n = 1000$ samples on each point in fuzzy space is implemented. Additionally, a surrogate model as described in section 4.3 with $n = 10^6$ simulations in total is also used. The resulting fuzzy-stochastic outputs are displayed for specimen type 1 in Figure 13 and for specimen type 2 in Figure 14, respectively.

Similar to the approaches under monomorphic uncertainties shown above, the experimental results are covered by the numerical predictions even if a shift to smaller ultimate loads F_max is present. The empirical fuzzy mean is almost completely inside the experimental range for specimen type 1. For specimen type 2, it is partly outside for smaller output membership function values, equivalent to larger deviations in the size parameters. Furthermore, the fuzzy CDF of specimen type 2 is steeper than of specimen type 1 which shows a smaller influence of the stochastic parameters (location and load angle) on the ultimate load. Also in the approach with polymorphic uncertainties, the application of the proposed surrogate based on ANNs is justified, comparing the numerical predictions with those from the classical sampling approach. The deviation is always negligible. The combination of stochastic

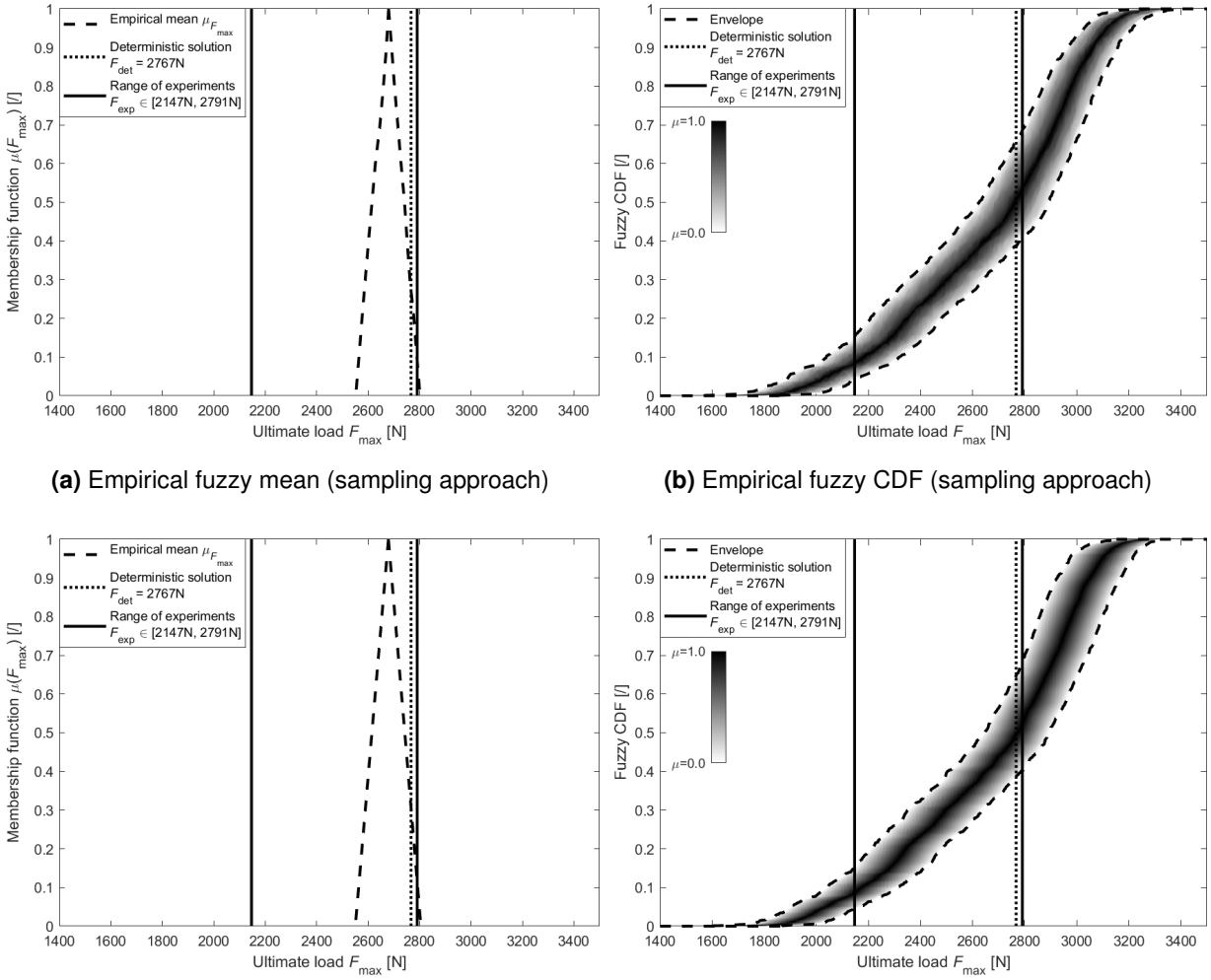

(a) Empirical fuzzy mean (sampling approach)

(b) Empirical fuzzy CDF (sampling approach)

(c) Empirical fuzzy mean (surrogate modeling)

(d) Empirical fuzzy CDF (surrogate modeling)

Figure 13: Fuzzy-stochastic output for specimen type 1.

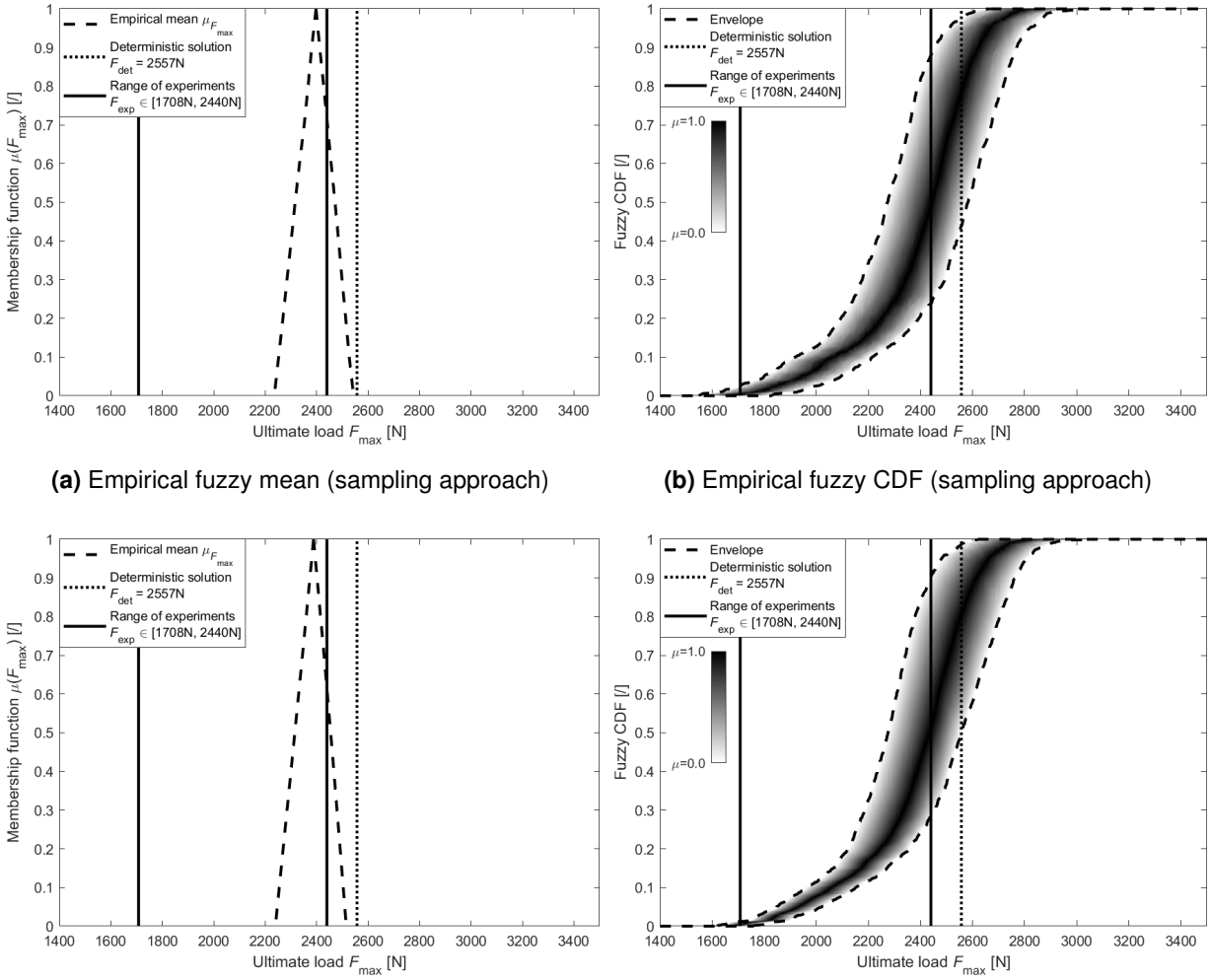

(a) Empirical fuzzy mean (sampling approach)

(b) Empirical fuzzy CDF (sampling approach)

(c) Empirical fuzzy mean (surrogate modeling)

(d) Empirical fuzzy CDF (surrogate modeling)

Figure 14: Fuzzy-stochastic output for specimen type 2.

and fuzzy variables allows the output evaluation on each stochastic sample regarding the fuzzy input parameters (size) and on each fuzzy sample regarding the stochastic input parameters (location and load angle). The simultaneous information about probabilities as well as possibilities (in terms of fuzzy sets) of the location of the maximum first principal stress concerning the ultimate load and the input uncertainties is an added value, see Figure 15.

The solutions for the deterministic size parameters in Figures 15a and 15c correspond to the solutions on the core ($\mu = 1.0$) of the fuzzy-stochastic output due to the definition of the size parameters as triangular fuzzy numbers. It is remarkable that these figures are almost identical to those in Section 5.1.1 which shows that the quantities of interest ($F_{\max}$ and $\mathcal{C}(\boldsymbol{x}_{\max})$) are nearly unaffected by the underlying uncertainty in the size parameters. Nevertheless, minor deviations like larger empirical means, smaller ranges of the stochastical output and steeper CDFs can be observed.

In contrast, $F_{\max}$ and $\mathcal{C}(\boldsymbol{x}_{\max})$ are sensitive to the location parameters and the load angle. For the deterministic location and load angle values given in Section 3, the fuzzy outputs in Figures 15b and 15d have been determined. Compared to the results in Section 5.1.2, solely the deterministic solutions on the core ($\mu = 1.0$) are equal. For specimen type 1, only one instead of four first crack locations is identifiable and the ultimate load $F_{\max}$ is now given in a smaller range of about $300\mathrm{N}$ on the support ($\mu = 0.0$). Also for specimen type 2, the amount of identified first crack locations is reduced, now from five to three, with a considerable smaller range of $F_{\max}$ as well. As a consequence, the output membership functions are slimmer which shows once more the minor influence of the size parameter uncertainty in the present applications.

6 Conclusions

The structural failure of perforated Plexiglas® plates was investigated experimentally and numerically in this contribution. Both the failure mechanism as well as the ultimate load are generally affected by uncertainties in material, geometry and boundary conditions. Different uncertainty models, monomorphic and polymorphic ones, have been applied successfully for the problem description with slightly different results. Within the polymorphic model, a combined statement about probabilities and possibilities also regarding the quantified inputs was shown. To overcome the high computational costs of the uncertainty propagation, a surrogate reponse method based on Artificial Neural Networks were employed in addition to classical sampling approaches. The numerical results for the ultimate loads, independent of the uncertainty description, cover the range of experimental ones that is generally expected. Furthermore, different locations of the maximum first principal stress can be depicted in the numerical simulations which lead to different failure mechanisms, detectable in the experiments. However, the range of numerical and experimental ultimate loads exhibit a shift. Consequently, other uncertainties like material inhomogeneities, thickness variation and hole shape irregularities have to be taken into account additionally in future considerations.

Acknowledgement

The authors gratefully acknowledge the financial support of the German Research Foundation (DFG) within the Priority Programme "Polymorphic uncertainty modelling for the numerical design of structures – SPP 1886".

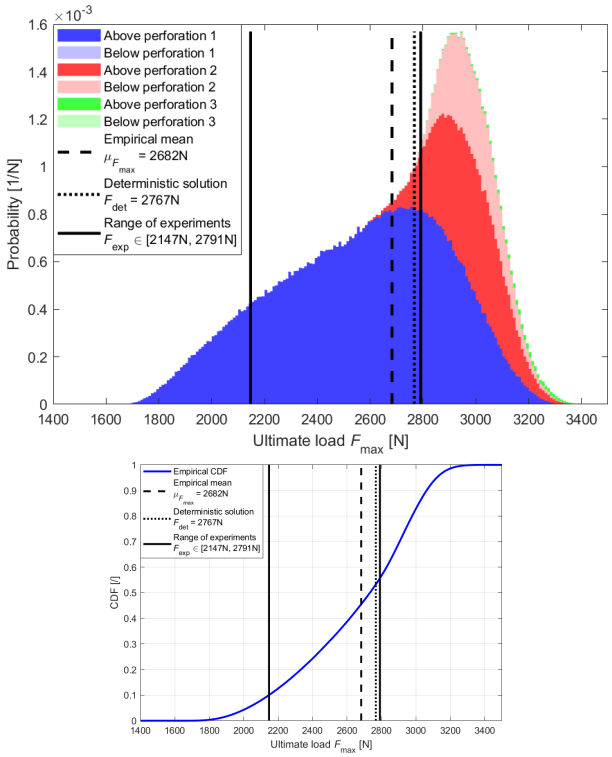

(a) Specimen type 1: stochastic output for deterministic size

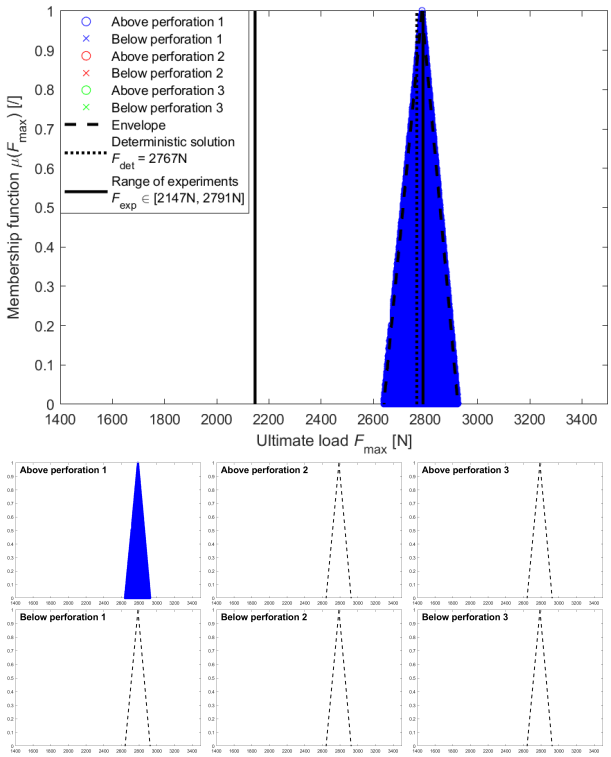

(b) Specimen type 1: fuzzy output for deterministic location without load angle scattering

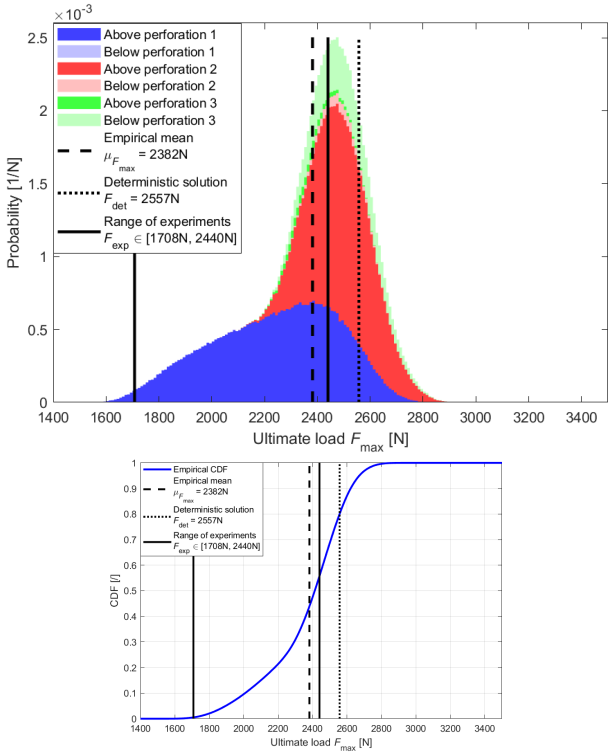

(c) Specimen type 2: stochastic output for deterministic size

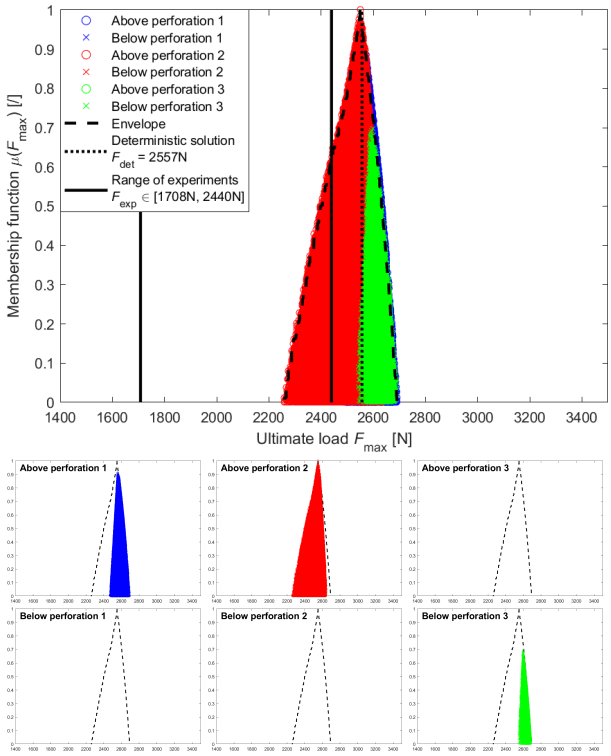

(d) Specimen type 2: fuzzy output for deterministic location without load angle scattering

Figure 15: Exemplary filtered pure stochastic and pure fuzzy outputs.

References

[1] F. Chollet et al. Keras. `https://keras.io`, 2015.

[2] DIN EN ISO 527-1:2012-06, Kunststoffe - Bestimmung der Zugeigenschaften - Teil 1: Allgemeine Grundsätze (ISO 527-1:2012), 6 2012.

[3] M. Eigel, R. Gruhlke, D. Moser, and L. Grasedyck. Low-rank surrogates for fuzzy-stochastic partial differential equations. *WIAS Preprint*, 2019.

[4] L. C. Evans. Partial differential equations. 2010.

[5] Evonik Industries AG. *Technische Information PLEXIGLAS®*, 1 2013. `https://www.plexiglas.de/sites/lists/pm/documentsap/211-1-plexiglas-gs-xt-de.pdf`; retrieved January 23, 2018.

[6] I. Goodfellow, Y. Bengio, A. Courville, and Y. Bengio. *Deep learning*, volume 1. MIT press Cambridge, 2016.

[7] W. Graf, M. Götz, and M. Kaliske. Analysis of dynamical processes under consideration of polymorphic uncertainty. *Structural Safety*, 52:194–201, 2015.

[8] M. Hanss. *Applied Fuzzy Arithmetic - An Introduction with Engineering Applications*. Springer, 2005.

[9] E. Kirsch. Die Theorie der Elastizität und die Bedürfnisse der Festigkeitslehre. *Zeitschrift des Vereines deutscher Ingenieure*, 42:797–807, 1898.

[10] A. N. Kolmogorov and A. T. Bharucha-Reid. *Foundations of the theory of probability: Second English Edition*. Courier Dover Publications, 2018.

[11] A. Krizhevsky, I. Sutskever, and G. E. Hinton. Imagenet classification with deep convolutional neural networks. In *Advances in neural information processing systems*, pages 1097–1105, 2012.

[12] O. P. LeMaître and O. M. Knio. *Spectral Methods for Uncertainty Quantification*. Springer, 2010.

[13] D. Moens and M. Hanss. Non-probabilistic finite element analysis for parametric uncertainty treatment in applied mechanics: Recent advances. *Finite Elements in Analysis and Design*, 47(1):4–16, 2011.

[14] B. Möller and M. Beer. *Fuzzy Randomness - Uncertainty in Civil Engineering and Computational Mechanics*. Springer, 2004.

[15] B. Möller and M. Beer. Engineering computation under uncertainty–capabilities of non-traditional models. *Computers & Structures*, 86(10):1024–1041, 2008.

[16] H. T. Nguyen. A note on the extension principle for fuzzy sets. *Journal of Mathematical Analysis and Applications*, 64(2):369–380, 1978.

[17] I. Papaioannou, M. Daub, M. Drieschner, F. Duddeck, M. Ehre, L. Eichner, M. Eigel, M. Götz, W. Graf, L. Grasedyck, R. Gruhlke, D. Hömberg, M. Kaliske, D. Moser, Y. Petryna, and D. Straub. Assessment and design of an engineering structure with polymorphic uncertainty quantification. *Surveys for Applied Mathematics and Mechanics (GAMM-Mitteilungen)*, 2019. (accepted).

[18] W. D. Pilkey and D. F. Pilkey. *Peterson's Stress Concentration Factors, Third Edition*. John Wiley & Sons, Inc., 2008.

[19] N.-P. Walz. *Fuzzy Arithmetical Methods for Possibilistic Uncertainty Analysis*. PhD thesis, Universität Stuttgart, 2016.

[20] C. Wang, Z. Qiu, and Y. He. Fuzzy stochastic finite element method for the hybrid uncertain temperature field prediction. *International Journal of Heat and Mass Transfer*, 2015.

[21] D. Xiu. *Numerical Methods for Stochastic Computation*. Princeton University Press, 2010.

[22] L. A. Zadeh. Fuzzy sets as a basis for a theory of possibility. *Fuzzy sets and systems*, 100(1):9–34, 1999.